Taylor & Francis
Taylor & Francis Group

Uncertainties in the inverse modelling of sulphur dioxide eruption profiles

PETRA SEIBERT*†, NINA I. KRISTIANSEN‡, ANDREAS RICHTER§,
SABINE ECKHARDT‡, ALFRED J. PRATA‡ and ANDREAS STOHL‡

†Institute of Meteorology, University of Natural Resources and Life Sciences (BOKU),
Vienna, Austria
‡Norwegian Institute for Air Research (NILU), Kjeller, Norway
§Institute for Environmental Physics, University of Bremen, Bremen, Germany

An inverse modelling methodology to derive vertical profiles of atmospheric
emissions in volcanic eruptions from satellite observations has been developed
and applied, inter alia, to sulphur dioxide from the Kasatochi 2008 eruption. In
this paper, the method is expanded to yield a posteriori uncertainties of the
emission profiles, and sensitivity experiments have been conducted to study the
influence of different assumptions for the input parameters. These parameters
are the a priori emission profile and its uncertainty, the uncertainties of the
observations, and the value of a smoothing parameter. The basic structure of
the emission profile with a tropospheric and a stratospheric peak, as well as the
heights of these peaks is very robust against the parameter variations. As
constraints on the inversion are loosened, the stratospheric peak becomes
stronger and sharper.

1. Introduction

The vertical mass distribution of gaseous and particulate emissions from volcanic
eruptions is an important but not very well known parameter. It is of crucial
importance to simulate and forecast the atmospheric transport of volcanic plumes.
Such forecasts are an important base of volcanic ash advisories issued operationally
by Volcanic Ash Advisory CentNGH (VAACs) (Prata 2009). In addition, climatic
effects of volcanic eruptions strongly depend on the injection height of the sulphur
dioxide that is emitted.

We have previously developed a methodology for retrieving vertical profiles of the
sulphur dioxide emissions in volcanic eruption columns. The method has so far been
applied to sulphur dioxide emissions from Jebel at Tair (Eckhardt *et al.* 2008),
Kasatochi (Kristiansen *et al.* 2010), and – in expanded form – Eyjafjallajökull (Stohl
et al. 2011). It is based on SO_2 satellite column data obtained during the hours and
days following the eruption, together with transport and dispersion calculations with
an atmospheric transport and dispersion model. These two sets of information are
used as input for an analytical inversion algorithm. The satellite data included were
GOME-2 (Global Ozone Monitoring Experiment-2, flown on the European MetOp

---

*Corresponding author. Email: petra.seibert@boku.ac.at

polar orbiting satellite), OMI (Ozone Monitoring Instrument, flown on the polar orbiting satellite AURA of NASA), SEVIRI (Spinning Enhanced Visible & InfraRed Imager, on the geostationary Meteosat Second Generation satellites), and AIRS (the Atmospheric Infrared Sounder on NASA's Aqua satellite) observations in different combinations, and we used the Lagrangian atmospheric transport model FLEXPART (Stohl *et al.* 2005).

The input required by the inversion consists of an a priori source profile together with its uncertainty, usually with a very simple shape, and the column values from the satellite retrieval, also with uncertainties. By the nature of the problem, the a priori information available for the emission profile is only a rough estimate – consequently we have developed a formal inverse method for its reconstruction. Its uncertainty is even more an ad-hoc, being an estimate determined as an 'educated guess'. The observation uncertainties are better known, but unfortunately they also need to represent the impact of errors in the atmospheric transport modelling, which again are only available as rough estimates. The main purpose of this paper is therefore to systematically study the impacts of different a priori assumptions on the a posteriori profiles and their uncertainties, using the case of the Kasatochi 2008 eruption.

So far, the method lacked a formal determination of the uncertainty of the reconstructed source profile. Here we introduce the algorithm for the calculation of this a posteriori uncertainty and discuss the results.

In this way, we improve confidence in this recently developed inverse modelling methodology for volcanic eruption plumes and its application to the urgent practical problems, especially in connection with respect to volcanic ash and aviation.

2. The Kasatochi 2008 eruption

The Kasatochi volcano is located on a small unpopulated island in the Aleutian arc of the northern Pacific Ocean (52.17° N, 117.51° W; background information is available from the Alaska Volcano Observatory[1]). The stratovolcano, which reaches only 314 m a.s.l., lay dormant for 200 years until the eruption in the summer of 2008. This eruption occurred in three pulses: 2008-08-07 22:01 UTC, 2008-08-08 01:50 UTC, and 04:35 UTC. The eruptions reached the stratosphere, with a plume top exceeding 15 km while the tropopause was at about 10 km (Kristiansen *et al.* 2010). All three eruption pulses emitted SO_2, a total of about 1.2–2.5 Tg (see quotes in Kristiansen *et al.* 2010), which is said to be the largest SO_2 mass loading since the Cerro Hudson 1991 eruption in Chile.

Our work is motivated not only by the wish to obtain quantitative estimates of the SO_2 mass injection profiles as a function of height, but also aims at improving volcanic ash predictions for air traffic warnings in the context of the SAVAA[2] project. The third eruption of the Kasatochi volcano was accompanied and followed by massive ash emission, and Alaska Airlines was forced to cancel 44 flights between 10 and 11 August 2008 (O'Malley and Holland 2008). The ash travelled along with the SO_2 for at least three days (Guffanti *et al.* 2010), thus SO_2 may also serve as a proxy for ash in this case. Making available improved methods for providing

---

[1]http://www.avo.alaska.edu/volcanoes/volcact.php?volcname=Kasatochi
[2]Support to Aviation for Volcanic Ash Avoidance (http://savaa.nilu.no/).

volcanic eruption source terms as a function of height and in a quantitative manner is one of the objectives of SAVAA.

3. Inverse modelling of the volcanic emission

3.1 *Basic methodology*

Kristiansen *et al.* (2010) have performed inverse modelling of the the SO$_2$ emission from Kasatochi with the methodology introduced in Eckhardt *et al.* (2008). The method is fully described in these two papers, and all the details of the application to Kasatochi including extensive validation are to be found in Kristiansen *et al.* (2010). Therefore, we will repeat only the most important key points necessary for following the results presented later on.

The method has three major components:

(i) SO$_2$ column values derived from satellite observations, in this case GOME-2 data (Richter 2009),
(ii) forward dispersion modelling with the Lagrangian particle model FLEX-PART (Stohl *et al.* 2005), and
(iii) an inversion procedure based on components (i) and (ii) (Seibert 1999, 2001; Eckhardt *et al.* 2008).

FLEXPART simulations with the derived source term have been compared with independent satellite observations of SO$_2$ at later dates, beyond the period used in the inversion, and LIDAR observations of aerosols from the CALIPSO (Cloud-Aerosol Lidar and Infrared Pathfinder Satellite Observations) satellite and from surface-based instruments, showing that the method works well. The forward and inverse modelling of the sulphur dioxide emission from Kasatochi as well as the comparison with independent data are also described in Kristiansen *et al.* (2010).

The present paper focuses on certain aspects of the inversion method in more detail. It systematically studies variations in adjustable input parameters (a priori emission profile, a priori uncertainties of both the first-guess emission profile and the satellite data), and it presents a posteriori uncertainties of the reconstructed emission profile. For simplification we use here only GOME-2 data as input, from four overpasses, of which two captured the whole plume (figure 1), the other two were on 8 August 22:56 UTC and 9 August 22:35 UTC. The GOME-2 SO$_2$ retrievals were selected as they are from a UV measurement which has sensitivity also to the lower troposphere and as they have been developed specifically for situations with very large SO$_2$ columns as found during the first days of the Kasatochi eruption. The larger columns from this retrieval should be more realistic than those from other observations as a larger part of the SO$_2$ column is included and no saturation is expected. Based on OMI observations, Krotkov *et al.* (2010) have derived a similar total SO$_2$ mass (2.2 Tg) from an extrapolation of the temporal evolution of the SO$_2$ decay, providing further support for the GOME-2 data used here.

To keep the set-up simple for this parameter variation study, we consider only the first of the three eruption pulses, implicitly ascribing all the sulphur dioxide release to this first pulse. Kristiansen *et al.* (2010) found that using ECMWF meteorological data as input to FLEXPART as we do here, the best results are obtained with the time of the first pulse. However, they have not attempted to do a time-resolved
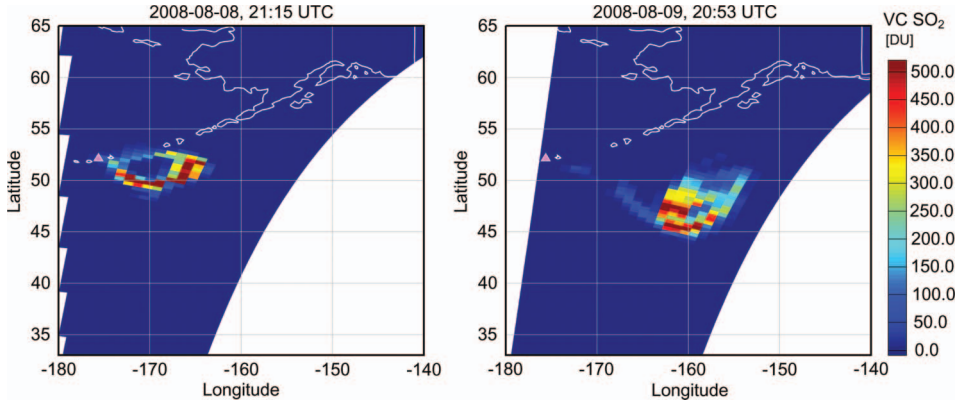
Figure 1. SO$_2$ column values retrieved from GOME-2 measurements for the two main overpasses. Kasatochi is marked by a pink triangle. Available in colour online.

inversion. Our methodology has only recently been expanded to include a temporal dimension in the source term (Stohl *et al.* 2011).

3.2 *Outline of the inversion procedure*

We consider m modelled column values of SO$_2$, **y**, with

$$\mathrm{y} = \mathrm{Mx} \tag{1}$$

where **x** is the vector of $x_1, \ldots, x_n$ source elements, and **M** is the $m \times n$ source-receptor sensitivity matrix. The observed values are denoted by y^{o}. The solution is obtained by minimizing a cost function J made up of three contributions, $J = J_1 + J_2 + J_3$. The contributing terms are

$$J_1 = (\mathbf{M}\tilde{\mathrm{x}} - \tilde{\mathrm{y}}^{\mathrm{o}})^{\mathrm{T}} \mathrm{diag}(\sigma_{\mathrm{o}}^{-2})(\mathbf{M}\tilde{\mathrm{x}} - \tilde{\mathrm{y}}^{\mathrm{o}}) \tag{2}$$

$$J_2 = \tilde{\mathrm{x}}^{\mathrm{T}} \mathrm{diag}(\sigma_{\mathrm{x}}^{-2})\tilde{\mathrm{x}} \tag{3}$$

$$J_3 = \varepsilon(\mathbf{D}\tilde{\mathrm{x}})^{\mathrm{T}}\mathbf{D}\tilde{\mathrm{x}} \tag{4}$$

Note that in the practical solution we make use of values with the first guess subtracted, which are denoted by $\tilde{x}, \tilde{y}$. J_1 measures the misfit between the modelled values and the observations, where σ_o are the standard errors of the observed column values. J_2 is a measure of the deviation from the a priori source profile with σ_x being its uncertainty expressed as standard error, and J_3 represents the deviation of the a posteriori profile from smoothness, ε being an adjustable weight for this contribution, and **D** a matrix operator for calculation of second derivatives, which are small for a smooth profile. The second and third term can be considered as a regularization to obtain a stable solution even if parts of the source are underdetermined, leading to an ill-conditioned problem. Minimization of J leads to a linear system of equations of size n (equation 5) that can be solved very quickly

with standard linear algebra tools. As this is an analytical solution, we can be certain of finding the global minimum of *J*.

The a posteriori source profile $\tilde{x}$ is obtained from

$$(\mathbf{M}^{\mathrm{T}} \operatorname{diag}[\sigma_{\mathrm{o}}^{-2}]\mathbf{M} + \operatorname{diag}[\sigma_{\mathrm{x}}^{-2}] + \varepsilon\, \mathbf{D}^{\mathrm{T}}\mathbf{D})\tilde{x} = \sigma_{\mathrm{o}}^{-2}\mathbf{M}^{\mathrm{T}}\tilde{y} \qquad (5)$$

or, using the abbreviation **G** for the matrix on the left-hand side,

$$\mathbf{G}\tilde{x} = \sigma_{\mathrm{o}}^{-2}\mathbf{M}^{\mathrm{T}}\tilde{y} \qquad (6)$$

In order to ensure a solution with only positive values, penalties are placed on negative values by increasing σ_x at the respective levels. This process is iterated until convergence.

The a posteriori uncertainties are obtained as (Menke 1984, Enting 2002: p. 174)

$$\sigma_{\mathrm{X}}^{\mathrm{b}} = \sqrt{\operatorname{diag}[\mathbf{G} + \operatorname{diag}(\sigma_x^a)^{-2}]^{-1}} \qquad (7)$$

Interpreting the inversion in statistical terms, the solution (a posteriori profile) represents the most likely profile, given both the a priori profile (which is 'projected' onto the observation space using the atmospheric transport modelling results) and the observations along with their uncertainties. Of course, it has also its own uncertainty which depends on the a priori uncertainties and the structure of the problem, and is less than the a priori uncertainty of the profile. The validity of the a posteriori uncertainty calculations depends on the same assumptions as the inversion itself, although referring to a second moment they are more susceptible to deviations from these assumptions.

While solving the linear system of equations in equation (6) does not require the explicit calculation of the inverse matrix **G**, we need this for the a posteriori uncertainties (equation 7). The calculation of the inverse matrix is accomplished with the LAPACK[3] routines SGETRF and SGETRI.

As already mentioned, some additional inputs beyond the observed values are needed:

(i)   observation uncertainties (σ_o) which represent measurement errors as well as the effects of atmospheric transport modelling uncertainties (σ_o was set to 20% of the observed value. A minimum value of 2 DU is applied to ensure a minimum uncertainty for near-zero observations, guided by the estimated retrieval uncertainty of at least 1 DU plus a rough value to represent the transport modelling error),

(ii) a priori values ($\mathbf{x}^a$),

(iii) their uncertainties (σ_x), and

(iv) the value of the smoothness parameter ε (empirical value).

In practice, the selection of the values of all these parameters necessarily depends, to some extent, on subjective judgments and estimations. Therefore, they are subject to the parameter variation experiments described in the next section.

---

[3]LAPACK is a free collection of linear algebra subroutines (see http://www.netlib.org/lapack/).

4. Parameter variation experiments and their results

An overview of the parameter variation experiments and their inputs is provided in table 1.

4.1 *The standard set-up*

The standard set-up assumes a smooth a priori distribution with a maximum just above the tropopause. A priori uncertainties follow the a priori profile but retain a minimum of 45 Mg m^{-1}. As result of the inversion, a bimodal profile with a tropospheric peak at 7 km and a stratospheric peak at 12 km is obtained (figure 2), with zero emissions resulting below 4 km and above 16 km. The uncertainties are greatly reduced relative to the a priori, now being only a few Mg m^{-1} – small compared to the two maxima which exceed 100 Mg m^{-1}. In order to suppress negative values, very small uncertainties for the a priori profile are implemented through an iterative process (Eckhardt *et al.* 2008). They penalize deviations from the a priori (which is always equal to or larger than zero) and thus practically prevent negative values. This iteration process affects mainly the upper part of the profile with near-zero a posteriori emissions. The total mass in the a priori emission profile is about 1.3 Tg, corresponding to retrievals from the OMI and AIRS satellite instruments (therefore it was used as the standard value in Kristiansen *et al.* 2010). The first GOME-2 overpass after 24 h had about 1.6 Tg and the second one after 27 h 2.7 Tg ($\approx$ 2.5 Tg according to table 1 in Kristiansen *et al.* 2010). This indicates saturation effects in the first overpass.

4.2 *Constant a priori*

The first sensitivity experiment is to assume that we know nothing about the profile and thus assume a vertically constant a priori emission (60 Mg m^{-1}), setting its

Table 1. Overview of parameter variation experiments. $\mathbf{x}^a$ refers to the a priori source profile, σ_x is the uncertainty of this profile, $\sigma_\mathbf{o}$ is the minimum uncertainty for the observations (a proportional uncertainty of 20% is always applied), and the value in the column ε is a factor for the weight for the smoothness condition.

Name (sub-section)	Figure	$\mathbf{x}^a$	σ_x	σ_o	ε
Standard set-up (4.1)	2	unimodal	$\geq$ 45 Mg m^{-1}[(1)]	2 DU	$\times 1$
Constant a priori (4.2)	3	60 Mg m^{-1}	=120 Mg m^{-1}	2 DU	$\times 1$
Small a priori uncertainty. (4.3)	4	60 Mg m^{-1}	=12 Mg m^{-1}	2 DU	$\times 1$
Large a priori uncertainty. (4.3)	5	60 Mg m^{-1}	=1200 Mg m^{-1}	2 DU	$\times 1$
Large a priori uncertainty with strong smoothness (4.3)	6	60 Mg m^{-1}	=1200 Mg m^{-1}	2 DU	$\times 100$
Large a priori uncertainty with weak smoothness (4.3)	7	60 Mg m^{-1}	=1200 Mg m^{-1}	2 DU	$\times 0.01$
Large minimum observation uncertainty (4.4)	8	60 Mg m^{-1}	=1200 Mg m^{-1}	20 DU	$\times 1$
A priori from constant first-guess profile (4.5)	9	result of figure 3	$10\mathbf{x}^{a(2)}$	2 DU	$\times 0.01$

[(1)]Otherwise variable, approximately 1.5$\mathbf{x}^a$. [(2)]With $\geq$10 Mg m^{-1}.
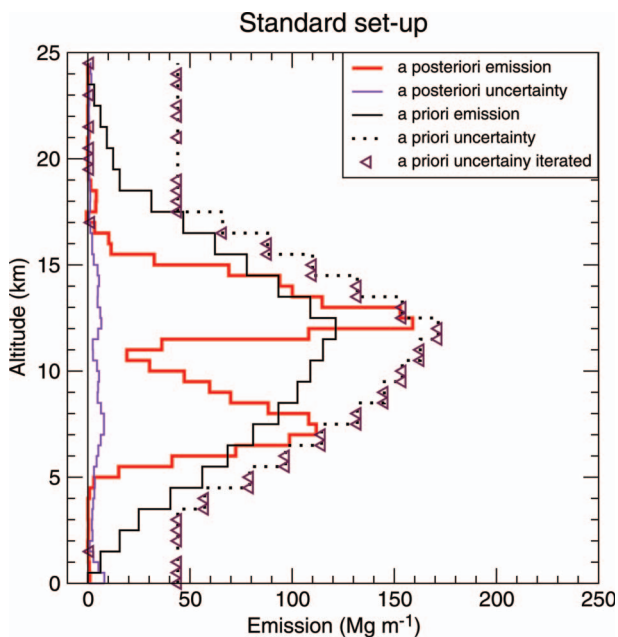
Figure 2. Vertical profiles of the a priori and a posteriori emission profiles and their uncertainties in the standard inversion set-up. The markers for 'a priori uncertainty iterated' show the standard deviation of the a priori profile after the iteration to suppress negative values in the a posteriori profile (see section 3.2).
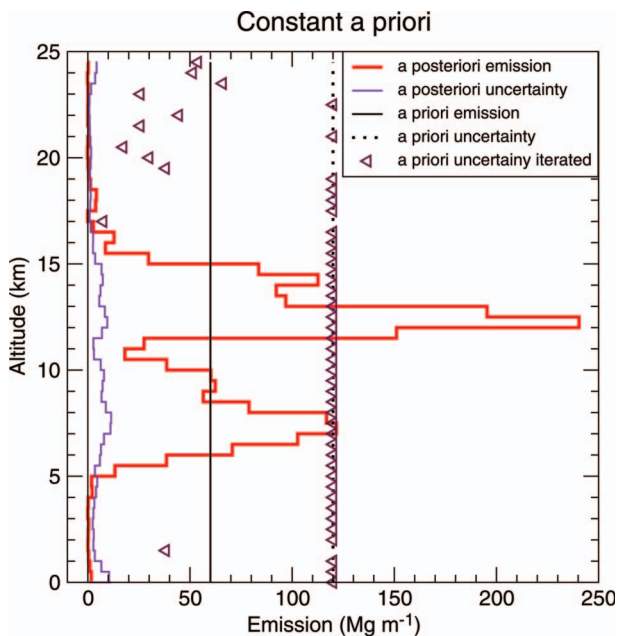
Figure 3. Like figure 2, but with a constant a priori emission profile of 60 and 120 Mg m^{-1} as uncertainty.

uncertainty to 120 Mg m^{-1} (figure 3). This set-up is also the baseline for the following experiments. The resulting height of the maxima and the region with zero emissions is identical to the standard set-up while the stratospheric peak becomes sharper and stronger. Both peaks show more structures but comparison with a posteriori uncertainties indicates that these structures are mostly noise (use e. g. $\pm 2\sigma$ as a yardstick for significance).

4.3 *Experiments with constant a priori and variation of the a priori profile uncertainties or the smoothness condition*

If the a priori uncertainties are reduced by one order of magnitude while keeping a vertically constant a priori (figure 4), amplitudes in the a posteriori profile are damped. This is to be expected because any large peak would be heavily penalized (the cost function contains the squared deviations between a priori and a posteriori). The peak emissions are much reduced and the stratospheric peak is only marginally larger than the tropospheric one, but the altitude of the maxima remains the same. The profile is also remarkably smooth. In addition, a spurious small maximum near the surface is introduced.

   If, on the contrary, the a priori uncertainties are increased by one order of magnitude above the standard, the resulting profile is expected to become more noisy, as is in fact observed in figure 5. The regularization to avoid negative values is invoked at more levels, including the region between the two peaks. The altitudes of the peaks are still unchanged but the stratospheric maximum becomes very sharp and almost reaches 500 Mg m^{-1}.

   If we keep the large a priori uncertainty but increase the smoothness parameter ε by a factor of 100 to regularize the inversion, the results (figure 6) are almost
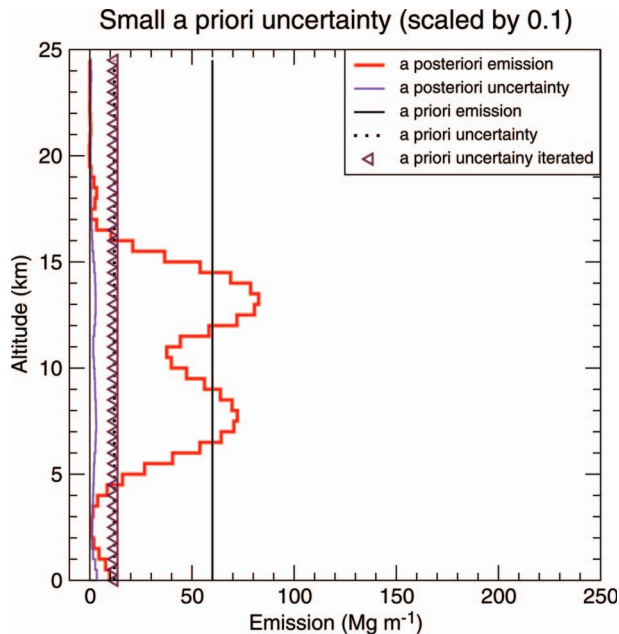
Figure 4.   Like figure 3, but a priori uncertainties reduced from 120 to 12 Mg m^{-1}.
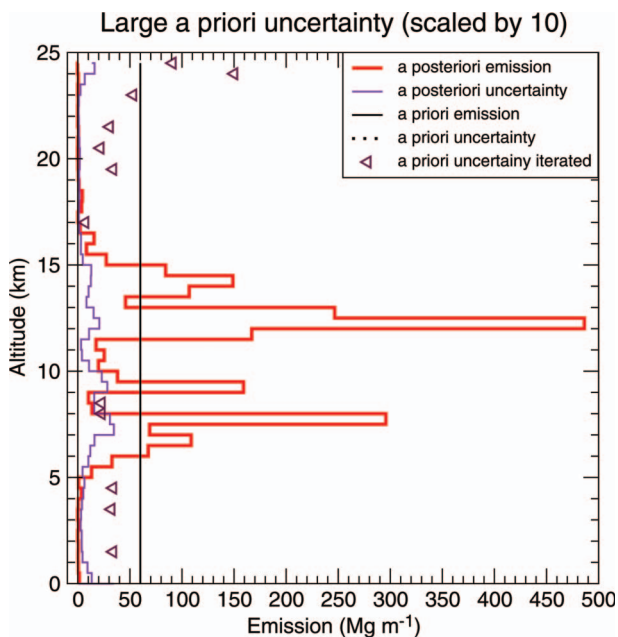
Figure 5. Like figure 3, but a priori uncertainties increased from 120 to 1200 Mg m^{-1}, thus outside the (enlarged!) scale.
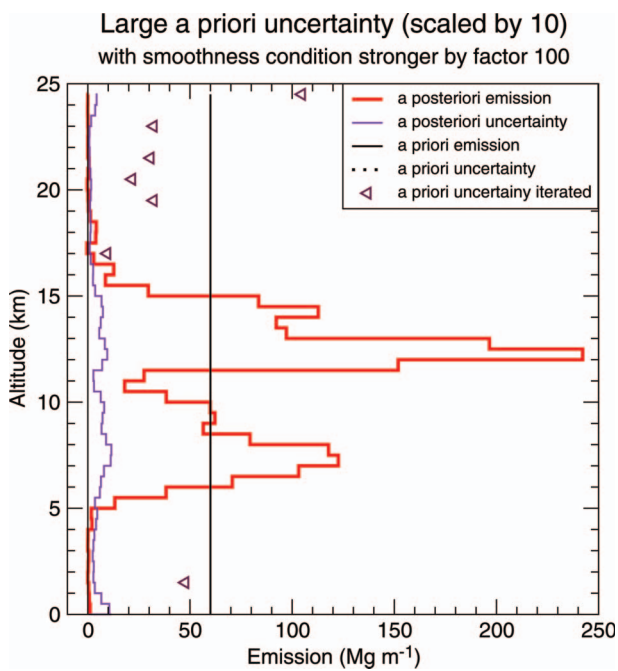
Figure 6. Like figure 5, but smoothness parameter ε is increased by a factor of 100.

identical to those obtained in the standard constant a priori case (figure 3), indicating that the smoothness condition and a smooth a priori profile together with a suitable uncertainty can have very similar effects.

If the value of the smoothness parameter ε is decreased by a factor of 100 compared to the standard value, the result (figure 7) is very similar to figure 5, indicating that the value of ε applied is already so small that compared to the other constraints it has only a small effect. In this case, a posteriori uncertainties rise up to 40 Mg m^{-1}.

4.4 *Variation of the observation uncertainties and total reconstructed mass*

In the numerical experiments discussed so far, the observation uncertainties are taken as the sum of 20% of the observation itself plus a value of 2 DU to avoid too strong constraints for (near-)zero observed SO_2 column values. In this numerical experiment, a minimum value of 20 DU has been set in addition to the standard uncertainty calculation. Under these conditions (figure 8), more mass is recovered, mainly through a broader tropospheric peak. Some spurious emissions close to the ground are also produced, but with large a posteriori uncertainty clearly indicating that this is not a trustable feature. While we didn't expect the GOME-2 data to be so uncertain, it is possible that the atmospheric transport calculations lead to position errors that could correspond to such values. Thus, this test can be considered a simplified approach to using quantified transport uncertainties. The value of 20 DU is still smaller than the uncertainty that has been assumed for the bulk of the plume where actual values are 200 to 500 DU, and thus uncertainties are 40 to 100 DU.
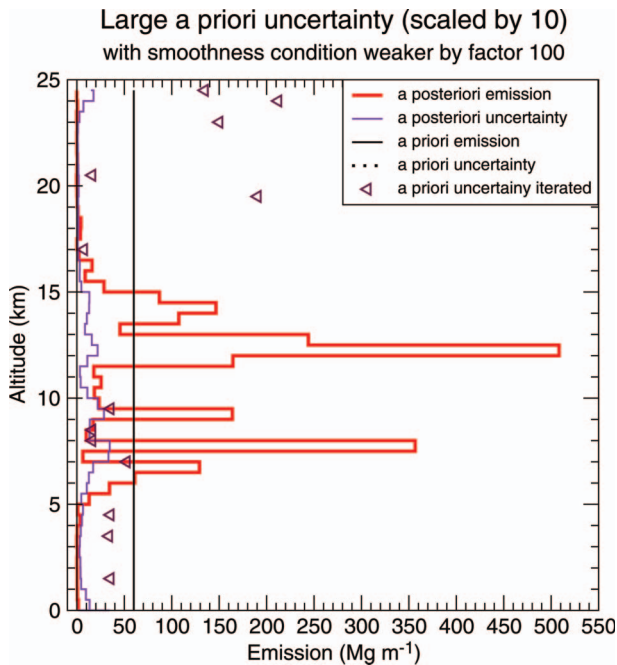
Figure 7. Like figure 5, but smoothness parameter ε is decreased by a factor of 100.

The total mass in the a posteriori profile, for given observation data, is sensitive mainly to the total mass in the a priori profile, but also to the observation uncertainties (table 2). If all overpasses are taken into account (which is done in all the set-ups considered in this paper, except the two at the bottom of the table), the
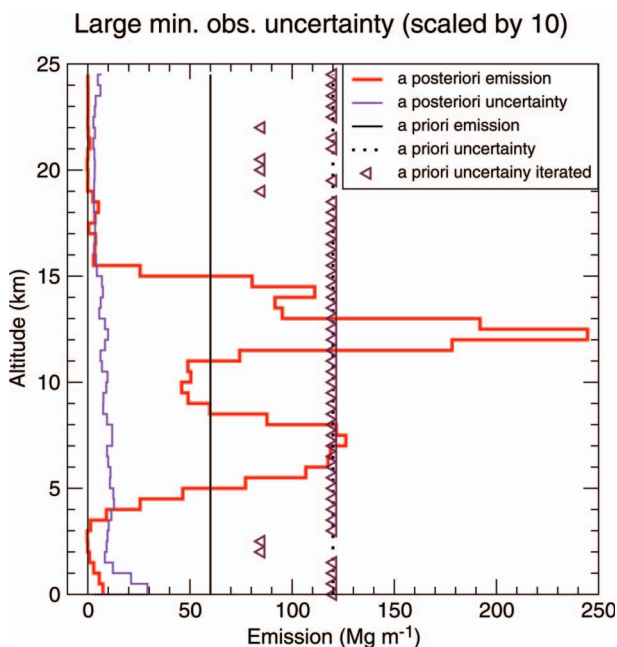
Figure 8.   Like figure 3, but minimum uncertainty for observations increased from 2 to 20 DU.

Table 2.   A posteriori total mass and correlation coefficient between observed and calculated column values of SO$_2$ for different set-ups.

Scenario	Total mass (Tg)		Correlation
	a priori	a posteriori	
All overpasses			
standard	1.3	0.85	0.65
standard	2.5	0.93	0.68
obsuncmx = 20DU	1.3	1.31	0.71
obsuncmx = 20DU	2.5	1.34	0.72
Only overpass at hour 47			
standard	1.3	1.31	0.71
standard	2.5	1.71	0.75
obsuncmx = 20 DU	1.3	1.99	0.76
obsuncmx = 20 DU	2.5	2.04	0.78

Note. 'standard' refers to the standard set-up as described in section 4.1; 'obsuncmx = 20DU' refers to a set-up where the observation uncertainty has been limited to 20 DU. The total a priori mass is also varied. The total mass in the observations is about 1.6 Tg in the first overpass and 2.7 Tg in the second overpass.

A priori from constant first-guess profile
weak smoothness
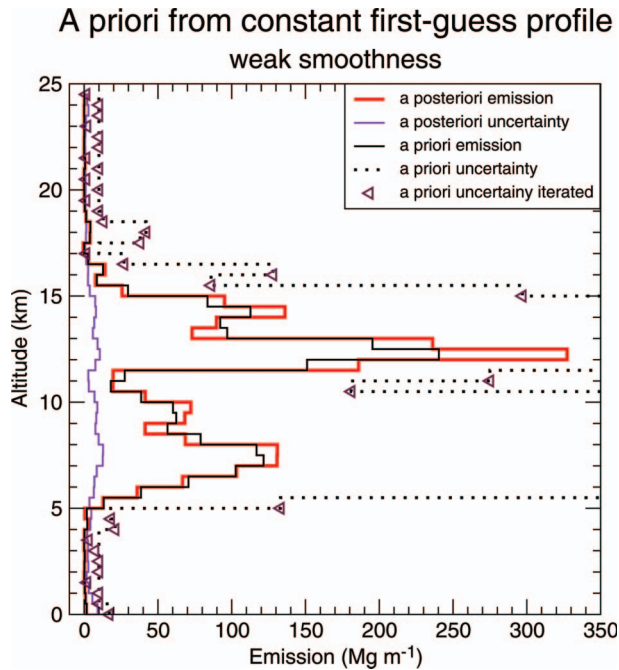
Figure 9.   A priori profile taken from the result of the inversion with simple assumptions (figure 3) uncertainties assumed to be a factor of 10 of those values, with a minimum of 10 Mg m^{-1}, smoothness parameter reduced by factor of 100.

a posteriori is 0.85 Tg in the standard case. Almost doubling the a priori mass increases the a posteriori mass by 10%. However, if the observation uncertainty is limited to 20 DU, which represents a massive reduction for the columns with the highest mass loadings, the a posteriori mass increases, as does the correlation. If we use only the second major overpass (at hour 47), the total a posteriori mass increases to 1.31 Tg for the standard case, which is still much less than the observed value. Correlations are larger, probably because it is easier to match the volcanic cloud at only one point in time but also at a later time when the cloud is a bit more spread out. In the case with 20 DU as an upper limit to the observation uncertainty and a priori total mass of 2.5 Tg, the a posteriori total mass reaches 2.04 Tg, better than the other results but still lagging behind the expectation. The increase in correlation by adopting a maximum uncertainty is easy to understand: reducing the observation uncertainty gives the term J_1 of the cost function a stronger weight, while the correlation is linked to this term which represents the (although weighted) mean squared error. One should also note that a lower correlation will tend to lower the a posteriori mass in the attempt to minimize this term J_1 where errors enter with power two, thus underestimations count less than overestimations. Applying an arbitrary upper limit for the observation uncertainty, as we have done here just to see its influence on the total mass, is not realistic, as it does have a roughly proportional component. The correct way forward would be to quantify the transport errors better, so that minor mismatches of the position for a sharp SO_2 feature would not lead to mass suppression.

4.5 *Iterating the first-guess profile*

All the parameter variations that give the inversion more freedom have so far led to sharper and stronger main peaks. All our first-guess choices were based on the assumption that we didn't know any details of the vertical emission structure. The results of the standard set-up as well as the parameter variation experiments show that there are two main peaks and that their heights are well defined. Thus, it seems promising to use this knowledge in another inversion – an a priori profile that is closer to reality should yield a more accurate result. We test this by taking the result of the most simple choice of the a priori, for which we had made no assumption about peak heights (section 4.2), and use the outcome (figure 3) as an input to another inversion. As we want to allow the inversion to still modify this result, we assume large a priori uncertainties. For the uncertainties of the emission profile, we take the a priori profile values (which were the results of the constant a priori case) times a factor of 10, with a minimum of 10 Mg m^{-1}, and reduce the smoothness parameter ε by a factor of 100. The main difference resulting from this a priori is an even sharper main peak in the a posteriori (figure 9). Additional regularization for removing negative values is invoked only in the upper part of the profile, while the spurious emissions close to the surface, present in the first guess, disappear.

5. Conclusions

Uncertainties of an inversion method to derive the vertical profile of the SO₂ source in the 2008 Kasatochi eruption using satellite measurements of SO₂ column values and an atmospheric transport model have been investigated. We have introduced the calculation of the a posteriori uncertainties of the emission profiles, and have conducted numerical experiments with variations of the different components of the a priori values needed as input to the inversion. The basic structure of the resulting profiles – a stratospheric and a tropospheric emission peak – and the heights of these peaks are very robust against all the parameter variations. Also, the regions devoid of emissions are robust. Note that according to Kristiansen *et al.* (2010) this holds as well with respect to changes in the satellite platform used for providing the observations, and is corroborated by comparison with observations of the plume height by LIDAR observations. This is a very positive result, although one has to be aware that it depends on the vertical wind shear, and thus is not guaranteed to work as well in other volcanic eruption cases. If statistical data in this respect are desired, numerical experiments with hypothetical volcanic emission profiles could be conducted for a selection of volcano sites around the world or in specific regions.

Whenever the regularization is weakened, the stratospheric peak of the Kasatochi emission profile becomes larger and sharper. This sharper peak is probably realistic, and should be taken into account for further refinement of the standard set-up. A possible way of doing this has been demonstrated by using in a first step an a priori that requires no knowledge about the vertical structure (i. e., it is vertically constant) and then use the results of this first inversion as first-guess in a second inversion step.

As long as more quantitative methods for determining a priori profiles and uncertainties are not available, it is important to use only observation-backed coarse features in its construction and to set the uncertainties large enough to allow relevant adjustments.

Errors in any part of the inversion, especially in the transport simulation, would lead to partly misaligned SO_2 cloud patterns and parts outside the observed cloud would be penalized. This effect cannot be corrected by adjusting the emission profile, but weaker emissions would in general limit the errors produced. This effect is similar to the reduced slope in a regression with low correlation. A larger observation uncertainty as in figure 8, which can be thought of as including a transport uncertainty contribution, counteracts this. Better quantification of transport uncertainty (Stohl *et al.* 1995; Seibert 2000, 2009; Stohl *et al.* 2011) should thus be helpful to obtain better inversions.

So far, saturation effects in the satellite observations and resulting differences in observed masses for different overpasses that typically are lumped together for the inversion have not yet received attention. Although the shapes of the retrieved profiles are quite robust, as shown in this paper as well as in Kristiansen *et al.* (2010), correction of input data with respect to the total mass should be explored in the future. Together with quantification of pixel-specific atmospheric transport errors, the regression employed for postprocessing of the simulated column values by Kristiansen *et al.* (2010) and Eckhardt *et al.* (2008) might then become unnecessary.

Within the SAVAA project, our method has also been extended to volcanic ash (Stohl *et al.* 2011). It has become obvious in the context of the Eyjafjallajökull spring 2010 eruption that a better definition of the source term could be very important for efficient support of VAAC operations, which came under heavy criticism from the aviation industry. Within the European Community a political decision was taken towards the implementation of quantitative ash thresholds. More quantitative methods with better accuracy for simulated ash concentrations are therefore needed, and our inversion method is a key contribution towards this aim. Specific eruption column models are not a good alternative. Especially in near-real-time and for volcanoes that are not monitored well, detailed knowledge of eruption source parameters is lacking. Furthermore, simple models are not very accurate (Stohl *et al.* 2011) while very complex models like ATHAM (Active Tracer High Resolution Atmospheric Model, Herzog and Graf 2010) are unsuitable for near-real time operations. Any simulation of gas or ash transport from a volcanic eruption, at the spatial scales for which the method is applicable, will benefit from our inversion results. This scale depends on the magnitude of the eruption column as its three-dimensional structure is ignored here, and on the resolution of the meteorological input available.

Continued cooperation between atmospheric modelling and remote sensing specialists should result in more detailed specifications of the observation uncertainties to be subsequently used in the inversion. At least equally important would be the quantification or at least characterization of the uncertainties arising from the atmospheric transport modelling.

References

ECKHARDT, S., PRATA, A.J., SEIBERT, P., STEBEL, K. and STOHL, A., 2008, Estimation of the vertical profile of sulfur dioxide injection into the atmosphere by a volcanic eruption using satellite column measurements and inverse transport modeling. *Atmospheric Chemistry and Physics*, **8**, pp. 3881–3897.

ENTING, I.G., 2002, *Inverse Problems in Atmospheric Constituent Transport* (Cambridge, UK: Cambridge University Press).

GUFFANTI, M., SCHNEIDER, D.J., WALLACE, K.L., HALL, T., BENSIMON, D.R. and SALINAS, L.J., 2010, Aviation response to a widely dispersed volcanic ash and gas cloud from the August 2008 eruption of Kasatochi, Alaska, USA. *Journal of Geophysical Research*, **115**, D00L19, doi:10.1029/2010JD013868.

HERZOG, M. and GRAF, H.F., 2010, Applying the three-dimensional model ATHAM to volcanic plumes: dynamic of large co-ignimbrite eruptions and associated injection heights for volcanic gases. *Journal of Geophysical Research*, **37**, L19807, doi:10.1029/2010GL044986.

KRISTIANSEN, N.I., STOHL, A., PRATA, A.J., RICHTER, A., ECKHARDT, S., SEIBERT, P., HOFFMANN, A., RITTER, C., BITAR, L., DUCK, T.J. and STEBEL, K., 2010, Remote sensing and inverse transport modeling of the Kasatochi eruption sulfur dioxide cloud. *Journal of Geophysical Research*, **115**, D00L16, doi:10.1029/2009JD013286.

KROTKOV, N.A., SCHOEBERL, M.R., MORRIS, G.A., CARN, S. and YANG, K., 2010, Dispersion and lifetime of the SO$_2$ cloud from the August 2008 Kasatochi eruption. *Journal of Geophysical Research*, **115**, D00L20, doi:10.1029/2010JD013984.

MENKE, W., 1984, *Geophysical Data Analysis: Discrete Inverse Theory* (Orlando, FL: Academic Press).

O'MALLEY, J. and HOLLAND, M., 2008, Planes flying again after ash cancellations. *Anchorage Daily News*, August 11. Available online at: www.adn.com/2008/08/11/490210/planes-flying-again-after-ash.html (accessed DD Month YYYY).

PRATA, A.J., 2009, Satellite detection of hazardous volcanic clouds and the risk to global air traffic. *Natural Hazards*, **51**, pp. 309–324.

RICHTER, A., 2009, Algorithm Theoretical Basis Document for the GOME-2 Rapid Volcanic SO$_2$ product. Available online at: http://www.dsas-bremen.de/so2_alerts/gome2_so2_atbd_091005.pdf (accessed 8 August 2011).

SEIBERT, P., 1999, Inverse modelling of sulfur emissions in Europe based on trajectories. In *Inverse Methods in Global Biogeochemical Cycles*, P. Kasibhatla, M. Heimann, P. Rayner, N. Mahowald, R.G. Prinn and D.E. HARTLEY (Eds), Geophysical Monograph Vol. 114, pp. 147–154 (Washington, DC: The American Geophysical Union).

SEIBERT, P., 2000, Uncertainties in atmospheric dispersion modelling and source determination. In *Proceedings of the Informal Workshop on Meteorological Modelling in Support of CTBT Verification*, 4–6 December 2000, Vienna, Austria.

SEIBERT, P., 2001, Inverse modelling with a Lagrangian particle dispersion model: application to point releases over limited time intervals. In *Air Pollution Modeling and its Application XIV*, F. SCHIERMEIER and S.E. GRYNING (Eds), pp. 381–390 (New York: Kluwer Academic).

SEIBERT, P., 2009, Current issues in atmospheric transport modelling and source location for the CTBT verification. In *Proceedings of the International Scientific Studies Conference (CTBTO/PrepCom)*, 10–12 June 2009, Vienna, Austria.

STOHL, A., FORSTER, C., FRANK, A., SEIBERT, P. and WOTAWA, G., 2005, Technical note – The Lagrangian particle dispersion model FLEXPART version 6.2. *Atmospheric Chemistry and Physics*, **5**, pp. 2461–2474.

STOHL, A., PRATA, A.J., ECKHARDT, S., CLARISSE, L., DURANT, A., HENNE, S., KRISTIANSEN, N.I., MINIKIN, A., SCHUMANN, U., SEIBERT, P., STEBEL, K., THOMAS, H.E., THORSTEINSSON, T., TØRSETH, K. and WEINZIERL, B., 2011, Determination of time- and height-resolved volcanic ash emissions and their use for quantitative ash dispersion modeling: the 2010 Eyjafjallajökull eruption. *Atmospheric Chemistry and Physics*, **11**, pp. 4333–4351.

STOHL, A., WOTAWA, G., SEIBERT, P. and KROMP-KOLB, H., 1995, Interpolation errors in wind fields as a function of spatial and temporal resolution and their impact on different types of kinematic trajectories. *Journal of Applied Meteorology*, **34**, pp. 2149–2165.